

Article

# Non-Linear Clumped Isotopes from DIC Endmember Mixing and Kinetic Isotope Fractionation in High pH Anthropogenic Tufa

Chris Holdsworth <sup>1</sup>, John MacDonald <sup>1</sup> and Cedric John <sup>2,\*</sup><sup>1</sup> School of Geographical and Earth Sciences, University of Glasgow, Glasgow G12 8QQ, UK<sup>2</sup> Department of Earth Science and Engineering, Imperial College London, London SW7 2AZ, UK

\* Correspondence: cedric.john@imperial.ac.uk

**Abstract:** Clumped isotope values ( $\Delta_{47}$ ) of carbonates forming in high pH conditions do not correspond to mineral precipitation temperatures due to certain effects including kinetic isotope fractionation and dissolved inorganic carbon (DIC) endmember mixing. Field-based archives of these carbonate environments are needed to evaluate and quantify these effects accurately. In this study, we measure the clumped isotope values of anthropogenic carbonates for the first time. Tufa layers were analyzed from samples precipitating in a high pH (>10) stream that drains a major slag heap in north east England.  $\Delta_{47}$  values are 0.044‰–0.183‰ higher than expected equilibrium values. Non-linear distribution of clumped isotope data is diagnostic of DIC endmember mixing, rather than partial equilibration of DIC. Episodic dilution of hydroxide-rich stream waters by equilibrated rainfall surface runoff provides the mechanism by which mixing occurs.  $\Delta_{47}$  values are ~0.010‰–0.145‰ higher than linear clumped isotope mixing profiles, suggesting that the majority of  $\Delta_{47}$  increase results from a combination of endmember non-linear mixing effects and an atmosphere-hydroxide sourcing of DIC. The diagnostic trends and variation in clumped isotope values present in these results demonstrates the potential of anthropogenic carbonate systems as a useful archive for studying and quantifying kinetic effects in clumped isotopes.

**Keywords:** tufa; anthropogenic carbonates; clumped isotopes; CO<sub>2</sub> hydroxylation; kinetic isotope fractionation; isotope disequilibrium

**Citation:** Holdsworth, C.; MacDonald, J.; John, C. Non-Linear Clumped Isotopes from DIC Endmember Mixing and Kinetic Isotope Fractionation in High pH Anthropogenic Tufa. *Minerals* **2022**, *12*, 1611. <https://doi.org/10.3390/min12121611>

Academic Editors: Francesca Giustini and Mauro Brilli

Received: 1 November 2022

Accepted: 10 December 2022

Published: 14 December 2022

**Publisher's Note:** MDPI stays neutral with regard to jurisdictional claims in published maps and institutional affiliations.



**Copyright:** © 2022 by the authors. Licensee MDPI, Basel, Switzerland. This article is an open access article distributed under the terms and conditions of the Creative Commons Attribution (CC BY) license (<https://creativecommons.org/licenses/by/4.0/>).

## 1. Introduction

### 1.1. Clumped Isotope Palaeothermometry

Clumped isotope analysis uses the abundance of <sup>13</sup>C-<sup>18</sup>O bonds in carbonate anions to measure mineral precipitation temperature. For carbonates forming in a system where water and composite dissolved inorganic carbon (DIC) pool are close to isotopic equilibrium, the occurrence of this heavy isotope clumping is inversely proportional to mineral precipitation temperature [1–6]. Clumped isotope values ( $\Delta_{47}$ ) correspond to excess mass 47 CO<sub>2</sub> measured during acid digestion of carbonates. These data are calibrated against carbonates precipitated at known temperatures [1,7–14], with increasing  $\Delta_{47}$  equating to decreasing mineral precipitation temperature. The ability to extract precipitation temperatures directly from carbonate mineral chemistry without any prior knowledge of parent water chemistry gives the clumped isotope method a significant advantage over conventional oxygen isotope palaeothermometry. As a result, there are now numerous examples of clumped isotope studies from across the earth sciences, covering topics including paleoclimate reconstruction [15–20], diagenetic histories [21–25], and fluid flow [26–28].

### 1.2. Non-Equilibrium Precipitation

There are certain carbonate-forming environments where equilibrium is not reached prior to mineral precipitation. Examples of this have been recorded at extremes of pH [29–34], temperature [16,35–38] and precipitation rates [5,39,40]. In these settings,  $\delta^{13}\text{C}$ ,  $\delta^{18}\text{O}$  and  $\Delta_{47}$  record disequilibrium effects; isotopic and kinetic processes that relate to solution chemistry and carbonate-forming reactions, rather than mineral precipitation temperatures [5,6,39–42].

#### Kinetic Isotope Effects

Carbonates precipitating rapidly in alkaline waters (pH > 10) at low temperatures (<30 °C) are likely to record kinetic isotope effects due to water-DIC equilibration times increasing with pH and decreasing with temperature [5]. In high pH conditions,  $\text{CO}_2$  is rapidly drawn in to the water column and converted into DIC via  $\text{CO}_2$  hydroxylation [31]. This kinetic process preferentially selects lighter isotopes ( $^{12}\text{C}$  and  $^{16}\text{O}$ ), depleting DIC in  $^{13}\text{C}$  and  $^{18}\text{O}$  [42–44]. Near-instantaneous carbonate precipitation prevents any isotopic equilibration between DIC and water, therefore preserving kinetic depletions in mineral bulk isotope signatures that are significantly below expected equilibrium values [31,32,34,45]. Our understanding of how these kinetic effects impact clumped isotopes is still in its infancy [6,46]. Depletions of  $^{13}\text{C}$  and  $^{18}\text{O}$  in high pH carbonates in Oman have corresponding enrichments in  $\Delta_{47}$  [33], with authors concluding  $\text{CO}_2$  hydroxylation also to be the cause of this. In this study, we investigate human-made (anthropogenic) carbonate deposits that form in similarly alkaline conditions and, in this instance, even lower temperatures (<20 °C). The independence of  $\Delta_{47}$  from growth rate above pH 10 means only kinetic disequilibrium effects should be recorded in these carbonates if the DIC speciation  $\Delta_{47}$  offset is corrected for [5,6,35,39,40,47–51].

### 1.3. Anthropogenic Carbonates

Anthropogenic carbonates typically form in the low temperature, high pH conditions described above. Weathering of human-sourced materials such as legacy industrial waste results in the liberation of divalent cations (e.g., Ca, Mg, and Fe) and hydroxide ( $\text{OH}^-$ ) into surface waters. These alkaline leachates promote rapid in-gassing and hydroxylation of atmospheric  $\text{CO}_2$ , followed by near-instantaneous carbonate precipitation [52,53]. A similar process of carbonate formation occurs through the weathering of natural silicate minerals in mafic and ultramafic rocks [33,34,54]. Accumulations of anthropogenic carbonates are recorded at banana plantations [55], quarries [56,57], landfill sites [58,59], furnace slag heaps [53,60–65] urban soils [52,66,67], and on cement [68,69] or concrete structures [70,71].

### 1.4. Purpose of Study

Our understanding of how kinetic effects impact  $\Delta_{47}$  is particularly hindered by a lack of field case study datasets from high pH, hydroxylation-related carbonate archives. This study tests anthropogenic carbonates as a useful archive for evaluating the impact of kinetic fractionations, such as  $\text{CO}_2$  hydroxylation, on  $\Delta_{47}$ . These clumped isotope values will be the first taken from human-derived carbonates.

Samples were collected from a high pH (>10) stream that drains a legacy slag heap on the outskirts of Consett in northeast England. Carbonate layers from up- and downstream samples were analysed and compared to historic environmental data (water temperature, flow, chemistry, etc. in [53,63,65,72]) to quantify the extent of clumped isotope disequilibrium. We expect  $\Delta_{47}$  values to record a kinetic enrichment from  $\text{CO}_2$  hydroxylation, combined with the product of any isotope endmember mixing processes.

## 2. Materials and Methods

### 2.1. Site of Study

Carbonate samples for this study were collected from the Howden Burn, a ~500 m stream that drains the main slag heap of the now-closed Consett Iron and Steel Works in northeast England (Figure 1A). The works was operational between the mid-19th century and 1980, producing ~120 Mt of steel and iron and >20 Mt of slag materials over its lifespan [53]. Slag was dumped in heaps surrounding the site (Figure 1B), as is captured by the westerly progression of heap deposits seen between 1880 and 1960 on historic map records (Supplementary Materials Figures S1–S7). The main heaps are underlain by alluvium and glacial till resting on top of Carboniferous mudstones [53]. Following the closure of the works the heaps were landscaped and redeveloped in the late 20th century. Recent estimates suggest the heaps reach a maximum thickness of 45 m and have a total volume of ~16 Mm<sup>3</sup> [53]. The constituents of the heaps vary substantially, with steel and iron slag, spoils, flue dusts, pot ashes and building demolition materials all being recorded as present [73]. Average compound composition of blast furnace and steel slag are reported in [63]. 314 tons of Ca is calculated to have leached from the main heap between 1980 and 2017 [53]. Based on CaO and MgO concentrations of heap constituents, this represents as little as 0.004% of the Ca present.

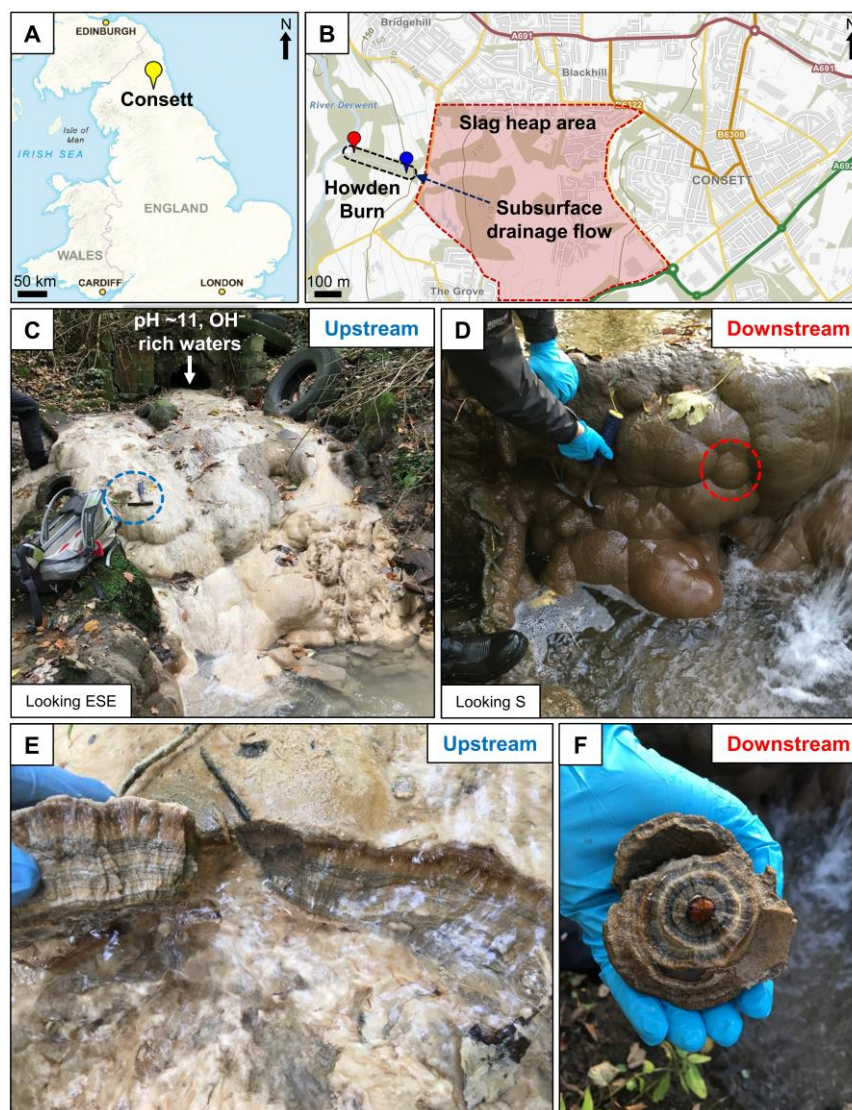


**Figure 1.** (A) Location of Consett in northeast England. (B) Area where slag deposition occurred during the lifespan of the steel and iron works. Red dashed area shows the extent of slag deposition

in Consett. Black dashed circle indicates the extent of the Howden Burn. Blue and red markers indicate the locations of upstream (blue) and downstream (red) samples on the Howden Burn. (C) Upstream tufa barrage located immediately after the Howden Burn emergence from slag heap subsurface drainage. Stream waters here are hyperalkaline (pH~11), rich in OH<sup>-</sup>, Ca and slag-derived metals. Upstream sampling point indicated by dashed blue circle. (D) Downstream tufa barrage located ~50 m before River Derwent confluence. Deposits are darker and harder than those found upstream. Downstream sample in-situ location indicated by dashed red circle. (E) In-situ picture of upstream sampling point showing mm-scale tufa layering; (F) Picture of downstream tufa sample showing tufa layer accumulation around a small stick.

### 2.1.1. Howden Burn

The Howden Burn drains the interior of the largest heap at Consett, emerging from a culverted subsurface drainage outflow on the western side of Pemberton Road. Historic map records document the direct infilling of the Howden Burn profile with slag between 1880 and the steelworks closure (Supplementary Materials Figures S1–S7). The culverted section from which the burn emerges follows the 1880 burn profile for ~150 m into the heap before ceasing on current drainage map records. The burn also receives leachate discharge from a surface water manhole cover which overflows to the immediate south east of the culvert emergence. Total burn catchment is measured at 0.68 km<sup>2</sup> and surface waters flow for ~500 m before reaching a confluence with the River Derwent [53].

The main hydrochemical characteristics of the Howden Burn are summarized in Table 1. Waters are hydroxide enriched and contain high loadings of Ca and metals leached from the heap contents [63,65]. Water temperature records from 1978–1999 range from 4 °C to 20 °C, with a median value of 10.3 °C [53]. Subsequent water temperature measurements record average values of 13.0 °C upstream and 12.8 °C downstream [72]. Burn pH records from 1978 to 1999 range from 6.5 to 12.7, with a median value of 11.0 [53]. Lower pH measurements (<9) present in this range correspond to measurements taken before slag heap redevelopment in the late 1990s and during periods when the burn was being actively dosed with acid to reduce surface water pH [53]. Following heap redevelopment non-slag leaching waters were redirected away from the burn via a combined sewer overflow pipeline [65]. This led to a change in burn catchment and a relative concentration of high pH (>10) slag leachate waters [65]. Subsequent water pH measurements throughout the 2000s show this higher pH has remained [65], with the most recent records showing average values of 11.6 upstream and 11.3 downstream [72].

**Table 1.** Major hydrochemical characteristics of Howden Burn discharge from [53] unless marked with \* [72]. Median values are shown with data ranges in brackets to highlight the concentration of high pH slag leachate in stream waters following heap redevelopment in the late 1990s.

Temperature (°C)	10.3 (4.4–20.0)
pH	11.0 (6.5–12.7)
Flow (l/s)	5.0 (2.5–10.0)
<b>Major Ions (mg/l)</b>	
Al	0.1 (<0.1–5)
Ca	150 (45–315)
Fe	1.6 (<0.1–4.7)
Mg	8.5 (3.3–13.9)
K	412 (143–688)
Na	172 (45–287)
Cl	67 (2–550)
SO <sub>4</sub>	755 (42–2700)
Total Alkalinity	162 (93–315)
OH <sup>-</sup> *	29 upstream, 13 downstream
CO <sub>3</sub> *	139 upstream, 20 downstream
HCO <sub>3</sub> *	9 upstream, 3 downstream

### 2.1.2. Carbonate Classification

Enrichment of  $\text{OH}^-$  and Ca in burn waters leads to substantial accumulations of  $\text{CaCO}_3$ , which precipitates via the formation of (bi)carbonate from the hydroxylation of atmospheric  $\text{CO}_2$  [53]. Precipitation rates have been calculated to range between 8 and 259  $\text{g/m}^2/\text{day}$  by dividing the difference in Ca mass loss at the leachate source and downstream by the sampling area (see [53] for full details). This is estimated to produce 11–117 kg of  $\text{CaCO}_3$  per day and 4–42 tons per year [53]. Such substantial volumes of precipitation results in extensive smothering of the stream channel and banks, increased opacity of the water column and accumulations of carbonate terraces, barrages and mini-cascade systems. The largest of these barrages is found immediately after the first emergence of the culverted watercourse (Figure 1C). Barrage size decreases downstream corresponding to changes in carbonate color and morphology.

Previous XRD analysis of Howden Burn carbonates indicates  $\text{CaCO}_3$  polymorphs aragonite and vaterite are present upstream but not downstream [63]. Precipitates are white-pale yellow upstream and resemble a soft, unlithified sediment. Downstream color darkens through orange to red-brown, and hardness increases towards that of a lithified carbonate rock (Figure 1C,D). Carbonates precipitating in the Howden Burn share characteristics indicative of tufas and travertines. The climatic and hydrological characteristics of the Howden Burn combined with the millimeter-scale laminations and cascade/barrage morphology of carbonates dictate that a tufa characterization is most appropriate for Howden Burn carbonates [74–77]. Tufa laminations vary from mm to cm scale, with intermittent dark clay layers and some darker carbonate layers, possibly indicating incorporation of local organic material (e.g., leaves from Howden Wood).

### 2.1.3. Samples

Tufa samples were taken from the Howden Burn in October 2017. For the purposes of this study five distinctive layers were analyzed from an upstream (CHS5; Figure 1E) and downstream (CHS16; Figure 1F) tufa sample. Sample CHS5 was taken from the largest tufa barrage in the Burn, located immediately after the emergence of leachate waters from the culvert. Sample CHS16 was taken from the last major tufa barrage before the Howden Burn-River Derwent confluence. Analyzing one tufa from either end of the Burn profile allows for a relative comparison between clumped isotope compositions upstream and downstream, whilst analyzing differing layers within each sample provides a relative measure of changes in clumped isotope compositions through the growth history of the sample (i.e., time). The five layers sampled from each tufa were labelled A–E, with 'A' corresponding to the youngest and outer-most layer, and 'E' corresponding to the oldest and inner-most layer (Supplementary Materials Figures S8 and S9). Due to the lack of absolute dating of tufa layers, adjacent layers were not always chosen for analysis. Instead, layers of differing color and morphology were chosen to assess for any impact these factors have on layer clumped isotope values.

## 2.2. Data Acquisition

### 2.2.1. Stable Isotope Measurements

$\delta^{13}\text{C}$ ,  $\delta^{18}\text{O}$  VPDB and  $\Delta_{47}$  clumped isotope measurements were made in the Qatar Stable Isotope Laboratory at Imperial College London in July 2018. A minimum of three replicates were analyzed from each tufa layer, using aliquots of 5–7 mg powdered sample in a randomized order. Replicates were analyzed using the automated Imperial Batch Extraction (IBEX) system. Individual samples were dropped into a vacuum-sealed common acid bath for reaction with 105% orthophosphoric acid for 10 min at 90 °C [78]. Acid digestion produces  $\text{CO}_2$  gas, which is then fed through a series of water, silver and Porapak-Q traps to remove water, sulfur and hydrocarbons respectively using He carrier gas [14,78–80]. This removes potential contaminants from  $\text{CO}_2$  gas, which is crucial given the nature abundance of mass 47  $\text{CO}_2$  is only 44 ppm [3,80].  $\text{CO}_2$  is captured in a second water

trap that is maintained at liquid nitrogen temperature, before being automatically loaded for analysis on a dual-inlet Thermo Fisher (Bremen, Germany) MAT 253 isotope ratio mass spectrometer [78,80].

Analytical protocols for the Imperial College lab are described in full in Dale et al. [21] and generally follow those outlined in Huntington et al. [79] and Dennis et al. [81]. The MAT 253 measures masses 44 to 49 of CO<sub>2</sub> simultaneously using modified collector arrays and uses an Oztech reference gas standard [80]. Each replicate measurement comprises eight acquisitions, with seven cycles per acquisition, each with an integration time of 26 s [78,80,82]. Measurements are repeated seven times per replicate in two different MAT 253 instruments, resulting in an analysis time of two hours per replicate on each mass spectrometer [78].

### 2.2.2. Data Analysis and Reduction

Clumped and bulk isotope data were corrected using the free software Easotope [82]. A pressure baseline correction, as described in Bernasconi et al. [83], was performed and  $\Delta_{47}$  data were then projected into the absolute reference frame, Carbon Dioxide Equilibrated Scale (CDES), of Dennis et al. [81]. This was carried out using a secondary transfer function based on measurements of ETH1, ETH2, ETH3, ETH4, and Carrara Marble (ICM) carbonate standards [14,84,85]. For this study, one standard was analyzed per three samples. Only samples with  $\Delta_{48}$  and  $\delta_{48}$  values that fall within 1‰ of the heated gas line ( $\Delta_{48}$  offset) and had a 49 parameter of <0.2 were accepted [14,82]. These signals were used as indicators for the presence of hydrocarbons, chlorocarbons and sulfur-bearing contaminants [78,79,86,87]. An acid fractionation factor of +0.082‰ [8] was added to the corrected  $\Delta_{47}$  data to bring data into the 25 °C scale used in calibrations. Results were then converted into temperature using the calibration of Davies and John [14], which is based on recalculated values from Kluge et al. [9] and new inorganic precipitates. This calibration accounts for updated <sup>17</sup>O parameters [88], is within analytical error of Bonifacie et al. [12] and the universal clumped isotope calibration of Kelson et al. [11], and includes the recent community inter-comparison efforts of Petersen et al. [13] regarding the <sup>17</sup>O correction and clumped isotope calibration. This study is mainly concerned with the impact of CO<sub>2</sub> hydroxylation on  $\Delta_{47}$ , therefore exact temperature calibration is not of paramount importance.

Data for each tufa layer corresponds to the average of replicate analyses, of which there were a minimum of three per layer. All  $\Delta_{47}$  values are reported in the CO<sub>2</sub> equilibrated scale [81] with 1 $\sigma$  as error, whilst measured  $\delta^{13}\text{C}$  and  $\delta^{18}\text{O}$  values are reported in the Vienna PeeDee Belemnite (VPDB) scale, also with 1 $\sigma$  as error. Average values for  $\delta^{13}\text{C}$  and  $\delta^{18}\text{O}$  VPDB replicates of standards fell within error of quoted values [84,85], except for  $\delta^{13}\text{C}$  for Carrara Marble (by 0.05‰) and  $\delta^{18}\text{O}$  for ETH4 (by 0.02‰). Average values for  $\Delta_{47}$  replicates of standards fell within error of quoted values for Carrara Marble and ETH3, but not ETH1 (by 0.007‰), ETH2 (by 0.022‰) or ETH4 (by 0.012‰). Full standards and samples datasets can be found in Research Data files deposited in the British Geological Survey (BGS) National Geoscience Data Centre (NGDC) at [89]. Clumped isotope temperature calculations are given in degrees centigrade with one standard error. A 95% confidence level for temperature values is also available in research data files. Source fluid  $\delta^{18}\text{O}$  values were calculated using the carbonate–water equilibrium fractionation factors of Kim and O’Neil [90] and are reported in the Vienna Standard Mean Ocean Water (VSMOW) scale with same errors as calculated temperatures. Due to the high pH of the Howden Burn these calculated fluid  $\delta^{18}\text{O}$  VSMOW values are not expected to provide an accurate estimate of parent solution  $\delta^{18}\text{O}$ . They are included to provide a comparison against regional seasonal  $\delta^{18}\text{O}_{\text{water}}$  data [91,92] and highlight the disequilibrium of carbonate precipitation in this environment.

### 2.3. Non-Linear Mixing Model

The non-linear mixing curves used to interpret clumped isotope data were derived using the non-linear mixing equation of Guo [6], formerly discussed by Defliese and Lohmann [93] and Eiler and Schauble [86]:

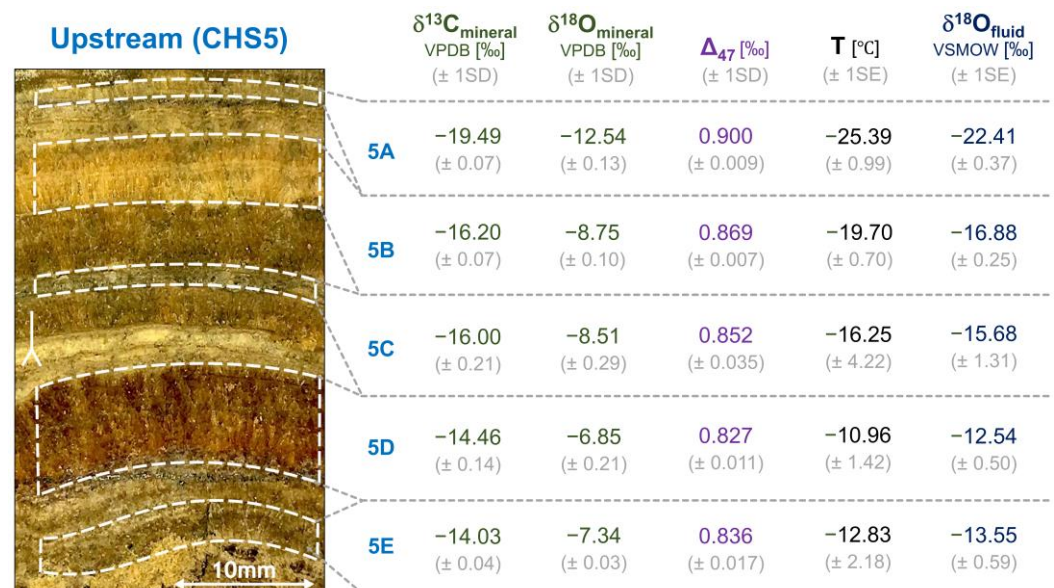
$$\Delta_{47,mix} \approx (1 - f) \times \Delta_{47,A} + f \times \Delta_{47,B} + f \times (1 - f) \times (\delta^{13}C_A - \delta^{13}C_B) \times (\delta^{18}O_A - \delta^{18}O_B) \quad (1)$$

where the *A* and *B* components are the equilibrium (lithogenic or biogenic) and disequilibrium (hydroxylation) endmembers respectively and *f* is the mixing ratio of endmember *B* component. Expected equilibrium clumped isotope values were calculated by reversing the  $\Delta_{47}$ -temperature conversion [14] for the historic water temperature range of the Howden Burn (4–20 °C; [53]), to give an expected equilibrium clumped isotope range of 0.708‰–0.763‰. Equilibrium carbonate mineral  $\delta^{18}O_{\text{mineral}}$  VPDB values under were calculated using regional meteoric rainfall values of Darling et al. [91], along with the carbonate-water equilibrium fractionation factor [90]. The disequilibrium used in the model corresponds to a carbonate sample from the hyperalkaline spring waters of the Semail ophiolite in Oman [33]. The near-identical bulk isotope values of this endmember sample ( $\delta^{13}C$  VPDB = −27.0‰;  $\delta^{18}O$  VPDB = −16.7‰) to the Dietzel et al. [32] hydroxylation bulk isotope values ( $\delta^{13}C$  = −25.3‰;  $\delta^{18}O$  = −17.6‰) makes this appropriate for the purposes of this study.

## 3. Results

### 3.1. Carbonate $\delta^{13}C$ and $\delta^{18}O$ Isotope Values

$\delta^{13}C$  and  $\delta^{18}O$  VPDB values of downstream tufa layers are generally lower than upstream layers (Figure 2). Layer 5A in the exception to this, with the lowest  $\delta^{13}C$  and  $\delta^{18}O$  VPDB values of the data set of −19.49‰ (±0.07‰) and −12.54‰ (±0.13‰) respectively. Upstream layer values range from −14.03‰ (±0.04‰) to −19.49‰ (±0.07‰) for  $\delta^{13}C$  VPDB and −6.85‰ (±0.21‰) to −12.54‰ (±0.13‰) for  $\delta^{18}O$  VPDB. Downstream values range from −15.94‰ (±0.02‰) to −18.65‰ (±0.25‰) for  $\delta^{13}C$  VPDB and −9.93‰ (±0.08‰) to −12.06‰ (±0.30‰) for  $\delta^{18}O$  VPDB.



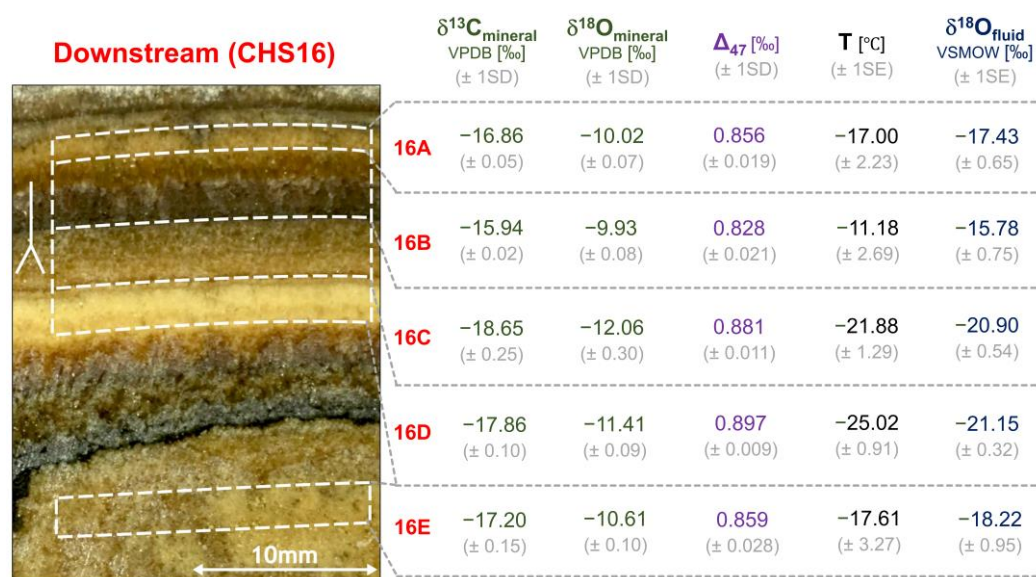


**Figure 2.** Bulk  $\delta^{13}\text{C}$  and  $\delta^{18}\text{O}$  VPDB isotope and  $\Delta_{47}$  clumped isotope results with corresponding temperature and  $\delta^{18}\text{O}_{\text{fluid}}$  VSMOW calculations for upstream (**top**) and downstream (**bottom**) tufa layers. Sample numbers 5A-5E and 16A-16E correspond to the hand specimen number from field sampling (5 and 16) and the youngest and outer-most layer (A), and the oldest and inner-most layer (E). White dashed lines indicate the layer and area from which each respective data point (e.g. 5A, etc.) was acquired. Errors are given in brackets and correspond to 1 standard deviation for bulk and clumped isotope data and 1 standard error for temperature and  $\delta^{18}\text{O}_{\text{fluid}}$  VSMOW data.

### 3.2. Carbonate $\Delta_{47}$ Clumped Isotope Values

Trends in clumped isotope data generally correspond to those present in bulk isotope data, meaning layers with lower  $\delta^{13}\text{C}$  and  $\delta^{18}\text{O}$  VPDB values have higher  $\Delta_{47}$  values. Exceptions to this trend are layers 16C ( $0.881 \pm 0.011\text{‰}$ ) and 16D ( $0.897 \pm 0.009\text{‰}$ ). Layer 5A has the highest  $\Delta_{47}$  value of the dataset ( $0.900 \pm 0.009\text{‰}$ ), whilst 5D the lowest ( $0.827 \pm 0.011\text{‰}$ ). Upstream values range between  $0.827\text{‰}$  ( $\pm 0.011\text{‰}$ ) and  $0.900\text{‰}$  ( $\pm 0.009\text{‰}$ ) and downstream values range from  $0.828\text{‰}$  ( $\pm 0.021\text{‰}$ ) to  $0.897\text{‰}$  ( $\pm 0.009\text{‰}$ ).

### 3.3. Calculated Temperatures and $\delta^{18}\text{O}_{\text{fluid}}$

Calculated temperature values for upstream and downstream data points correspond to the trends seen in  $\Delta_{47}$  values (Figure 2). Upstream layer temperatures range from  $-25.39\text{ °C}$  ( $\pm 0.99\text{ °C}$ ) to  $-10.96\text{ °C}$  ( $\pm 1.42\text{ °C}$ ) and downstream temperatures range from  $-11.18\text{ °C}$  ( $\pm 2.69\text{ °C}$ ) to  $-25.02\text{ °C}$  ( $\pm 0.91\text{ °C}$ ).  $\delta^{18}\text{O}_{\text{fluid}}$  VSMOW values derived from  $\delta^{18}\text{O}_{\text{mineral}}$  VPDB and  $\Delta_{47}$  show ranges of  $-12.54\text{‰}$  ( $\pm 0.50\text{‰}$ ) to  $-22.41\text{‰}$  ( $\pm 0.37\text{‰}$ ) for upstream layers and  $-15.78\text{‰}$  ( $\pm 0.75\text{‰}$ ) to  $-21.15\text{‰}$  ( $\pm 0.32\text{‰}$ ) for downstream.

## 4. Discussion

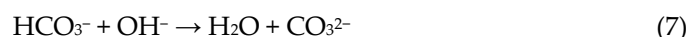
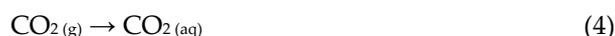
Carbonate clumped isotope temperatures calculated in this study are  $\sim 20\text{--}35\text{ °C}$  colder than the Howden Burn median water temperature of  $10\text{ °C}$  (Table 1). This substantial negative offset corresponds to higher  $\Delta_{47}$  clumped isotope and lower bulk  $\delta^{13}\text{C}$  and  $\delta^{18}\text{O}$  VPDB values, relative to those expected for carbonates precipitating at Howden Burn water temperatures ( $4\text{--}20\text{ °C}$ ). Calculated  $\delta^{18}\text{O}_{\text{fluid}}$  VSMOW values are comparably offset from regional values of  $-8.2\text{‰}$  (winter) and  $-7.0\text{‰}$  (summer) [91,92]. Using the historic temperature range above and the  $\Delta_{47}$ -temperature calibration of Davies and John [14], clumped isotope values are  $0.044\text{‰}$ – $0.183\text{‰}$  higher than expected. Given that clumped isotopes have provided accurate and reliable reconstructions of carbonate mineral precipitation temperatures in other temperate European [10] and Japanese [94] tufas, isotope data offsets in this study must be caused by hydrochemical characteristics of the Howden Burn that differ to that of the examples above.

#### 4.1. High pH Carbonates

The dominant characteristic of the Howden Burn hydrochemical environment is high pH (Table 1). Measurements regularly exceed pH 11, compared to pH < 9 in the European and Japanese tufa studies [10,94]. High pH values result from the leaching of slag minerals such as larnite (Equation (2)) and portlandite (Equation (3)), which enriches Howden Burn waters in hydroxide (OH<sup>-</sup>) and divalent cations (e.g., Ca):



This creates a specialized carbonate forming environment that differs from the majority of carbonate archives. OH<sup>-</sup> abundance promotes in-gassing and absorption of atmospheric CO<sub>2</sub> into the water column, where newly formed (bi)carbonate then reacts with leached Ca to rapidly precipitate calcium carbonate (CaCO<sub>3</sub>) [32,51]:



##### 4.1.1. DIC Speciation

There are two significant consequences of this carbonate forming process for clumped isotope values. First, the speciation of composite DIC changes with solution pH [39,41]. Above pH~10.3, dominant speciation transitions from bicarbonate (HCO<sub>3</sub><sup>-</sup>) to carbonate (CO<sub>3</sub><sup>2-</sup>), meaning DIC speciation in high pH environments such as the Howden Burn differs from that of lower pH, 'natural' carbonate precipitating environments (e.g., Kato et al. [94]; Kele et al. [10]). Speciation of DIC is known to produce certain offsets in clumped isotope values [5,39,41]. For a system such as the Howden Burn, which is pH > 10.3 and CO<sub>3</sub><sup>2-</sup> dominated (see Table 1), Δ<sub>47</sub> values are offset by up to -0.05‰ [5,39,41]. This is the opposite to the trend seen in Howden Burn tufa data, which suggests DIC speciation is not responsible for higher clumped isotope values in Howden Burn tufas.

##### 4.1.2. CO<sub>2</sub> Hydroxylation

The second consequence of this carbonate forming process for clumped isotope values relates to the source of DIC and the process by which CO<sub>2</sub> moves from the atmosphere into carbonate minerals. The in-gassing of CO<sub>2</sub> produces a kinetic isotope fractionation during the reaction between aqueous CO<sub>2</sub> and OH<sup>-</sup> (Equation (7)), known as CO<sub>2</sub> hydroxylation. This produces a stable isotope enrichment factor of -18.8‰ for δ<sup>13</sup>C VPDB [32,51,95] and -13‰ for δ<sup>18</sup>O VPDB [96,97] in the resultant DIC pool. Abundant supply of cations then allows for near-instantaneous carbonate precipitation (Equation (8)). This, combined with the substantial time requirements for isotopic equilibration at low temperature and high pH (>10<sup>6</sup> min) means tufa layers inherit isotopic signals that correspond to the kinetic fractionation of CO<sub>2</sub> and atmosphere-hydroxide sourcing of DIC, rather than mineral precipitation temperatures [5,6,39,98,99]. These signals are referred to as clumped isotope disequilibrium effects.

Evidence of this isotopic disequilibrium is recorded in previous studies of Consett slag-derived carbonates. Strong depletions of <sup>13</sup>C and <sup>18</sup>O in Howden Burn tufas [53] and other carbonate morphologies [52] are diagnostic of an atmospheric CO<sub>2</sub> source and hydroxylation disequilibrium effects. Carbonates precipitating in hyperalkaline springs in Oman record comparably negative bulk isotope values [33]. Clumped isotope compositions were also measured for these carbonates and yield values up to 0.200‰ higher than

those expected for equilibrium precipitation [33]. This is comparable to the offset of  $\Delta_{47}$  values seen in this study, which given the differing climates and ambient temperatures of northern England and Oman highlights the lack of temperature correspondence of clumped isotope compositions in high pH carbonates.

#### 4.2. Variation in Disequilibrium

Variation in clumped and bulk isotope values suggests the rate or extent of  $\text{CO}_2$  hydroxylation and/or carbonate precipitation in the Howden Burn is changing. In high pH environments such as this, carbonate precipitation rate is defined as:

$$r = C_o \times (D \times k \times [\text{OH}^-])^{0.5} \quad (9)$$

where  $C_o$  is the  $\text{CO}_2$  concentration in solution ( $\text{mol cm}^{-3}$ ),  $D$  is the diffusion coefficient of  $\text{CO}_2$  through a liquid ( $\text{cm}^2 \text{s}^{-1}$ ),  $k$  is the rate constant for hydroxylation ( $\text{cm}^3 \text{mol}^{-1} \text{s}^{-1}$ ) and  $\text{OH}^-$  is the hydroxide concentration in solution ( $\text{mol cm}^{-3}$ ) [32,51,100]. If standard values for  $D$  ( $10^{6.41} \text{cm}^2 \text{s}^{-1}$ ) and  $k$  ( $10^{-4.83} \text{cm}^3 \text{mol}^{-1} \text{s}^{-1}$ ) are assumed, then the primary rate-controlling step of carbonate precipitation is the hydroxylation of dissolved  $\text{CO}_2$  gas [52]. Hydroxylation requires the supply of  $\text{CO}_2$  and  $\text{OH}^-$  to stream waters, therefore factors that interrupt or change the availability of either will impact upon the extent of tufa isotopic disequilibrium.

##### 4.2.1. Supply of $\text{CO}_2$

Supply of  $\text{CO}_2$  has increased since the onset of tufa precipitation (~1880) due to increasing atmospheric  $\text{CO}_2$  concentrations from the burning of fossil fuels [101]. The subsequent increased greenhouse effect and planetary warming decreased atmospheric  $\text{CO}_2$   $\delta^{13}\text{C}$  by ~1.5‰ in the 20th century [102]. The magnitude of this change is much smaller than the disequilibrium and intra-dataset variation of isotope values seen in this study. Further, if  $\text{CO}_2$  supply was responsible for the variation in isotope data, the extent of isotopic disequilibrium should decrease with layer age. In the upstream sample the exact opposite is recorded, with  $\delta^{13}\text{C}$  and  $\delta^{18}\text{O}$  VPDB values decreasing and  $\Delta_{47}$  values increasing along growth (Figure 2). The layers sampled in this tufa are not adjacent either, meaning that this trend may not be representative of the overall trend with layer age. This point is emphasized by the lack of a unidirectional trend in isotope values for the adjacent layers measured in the downstream sample (Figure 2). Together this suggests that increased supply of  $\text{CO}_2$  from anthropogenic emissions is not responsible for variation in layer values.

##### 4.2.2. Supply of $\text{OH}^-$

Previous studies of Howden Burn hydrochemistry have highlighted the inverse correlation between stream water pH and carbonate precipitation [63,65]. This suggests that whilst the supply of  $\text{OH}^-$  has remained relatively constant, its relative concentration in the Howden Burn varies due to dilution from rainfall surface runoff. During periods of high rainfall dilution is at its most extreme, reducing stream pH and thus the capacity for  $\text{CO}_2$  hydroxylation and subsequent carbonate precipitation (as per Equation (9)). Mixing of circumneutral meteoric waters also supplies stream waters with non-hydroxylation related DIC that is already equilibrated to ambient temperature conditions. As a result, carbonates that precipitate during periods of higher rainfall and dilution record bulk and clumped isotope signatures trending back towards that of expected equilibrium values [33].

#### 4.3. Endmember Mixing

The seasonal, daily, and sometimes hourly fluctuations of rainfall and subsequent dilution of hydroxide in the Howden Burn results in a distribution of tufa isotope data along bulk and clumped isotope mixing trends. This produces a linear spread of  $\delta^{13}\text{C}$  and  $\delta^{18}\text{O}$  VPDB data between disequilibrium and equilibrium endmembers (see Figure 3). The

disequilibrium endmember corresponds to a hydroxylation endmember ( $\delta^{13}\text{C} = -25.3\text{‰}$ ,  $\delta^{18}\text{O} = -17.6\text{‰}$ ) [32]. There are two potential equilibrium endmembers for the Howden Burn; lithogenic ( $\delta^{13}\text{C} = 0\text{‰}$ ,  $\delta^{18}\text{O} = 0\text{‰}$ ) [53] or biogenic ( $\delta^{13}\text{C} = -8.0\text{‰}$ ;  $\delta^{18}\text{O} = -6.8\text{‰}$ ) [103]. Previous studies of Howden Burn carbonates have assumed a lithogenic endmember for calculating  $\text{CO}_2$  sequestration rates in the stream [53]. If the same approach is applied to bulk isotope data presented here, tufas contain 55%–77% atmospheric  $\text{CO}_2$ . This is lower than the 80% average in Mayes et al. [53] but within the overall range, therefore supporting  $\text{CO}_2$  sequestration estimates for the stream.

Given there is no significant source of lithogenic carbon in the Howden Burn's catchment and the stream itself is surrounded by woodland, we suggest a biogenic equilibrium endmember may be more suitable for this carbonate system. The proximity of the woodland around the stream means that rainfall runoff and surface waters interact with significant quantities of biogenic carbon prior to entering the burn, particularly in higher rainfall months. Trends in isotope data relating to tufa layer color support this mechanism of carbon sourcing. Darker layers tend to record lesser extents of carbonate isotope disequilibrium. Assuming darker layers correspond to those rich organic materials, this suggests the main source of equilibrium, or non-hydroxylation related carbon, is biogenic rather than lithogenic. In this scenario, the proportion of atmospheric  $\text{CO}_2$  in these tufas is  $\leq 50\%$ , which implies the  $\text{CO}_2$  sequestration estimates of Mayes et al. [53] are towards the upper limit of plausibility.

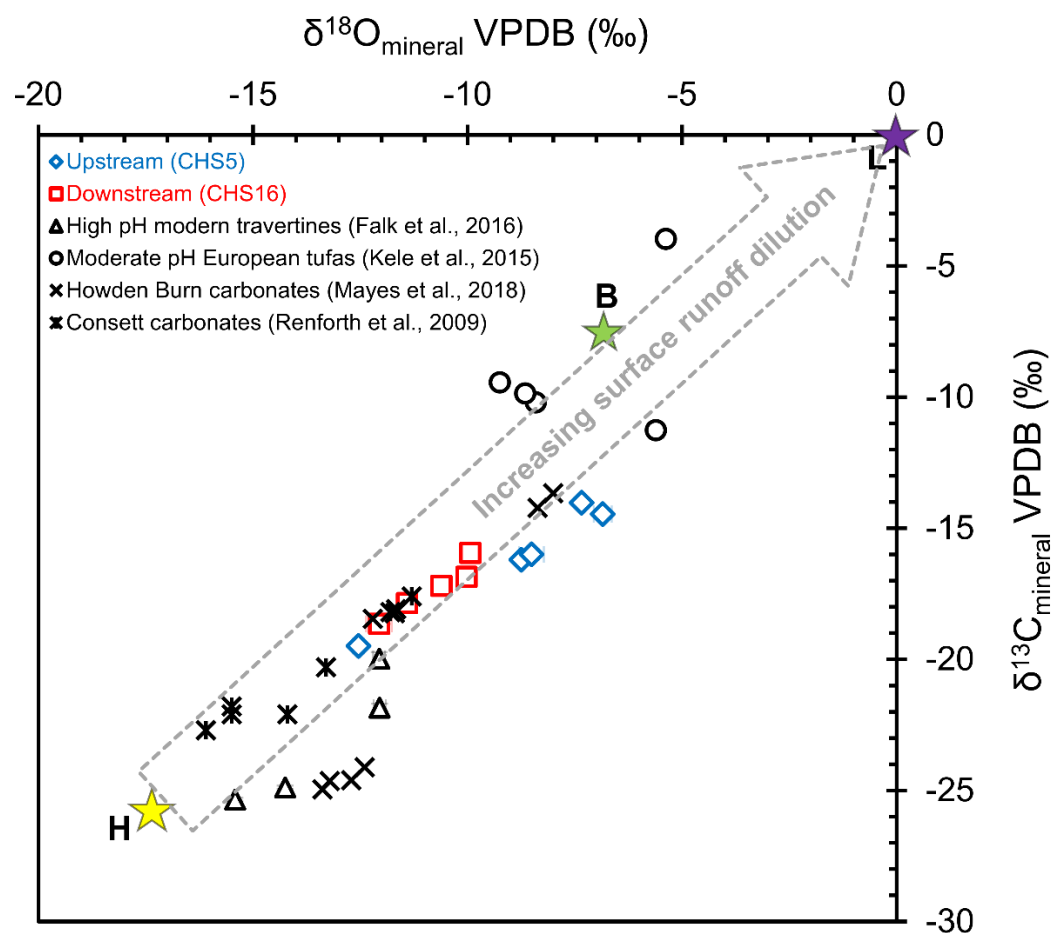


**Figure 3.** Plot of up- and down-stream tufa layer bulk  $\delta^{13}\text{C}$  and  $\delta^{18}\text{O}$  VPDB isotope data. Results from previous Consett carbonates [52,53], hyperalkaline modern travertines [33] and temperate circumneutral tufas [10] are also shown, along with values for hydroxylation (H; yellow star, from [32]), biogenic (B; green star, from [103]) and lithogenic (L; purple star, from [52,56]) isotope endmember values. Arrow shows linear mixing trend of data, which for Howden Burn carbonates corresponds to the variable extents of surface runoff dilution of hyperalkaline leachate waters.

### Non-Linear Mixing

The linear mixing trend of bulk isotopes evident in Figure 3 could alternatively be interpreted as partial equilibration of DIC prior to carbonate precipitation, shifting isotope values back towards those expected from equilibrium precipitation. We know this to be unlikely due to the low temperature, high pH conditions in the Howden Burn, and the records of rapid precipitation rates [53]. However, the point remains that bulk isotope data alone cannot empirically rule out partial equilibration. The distribution of clumped isotope data (Figure 4) can provide this quantitative evidence. If partial equilibration of DIC were responsible for variation in isotope data, one would expect to see a linear mixing trend between equilibrium and hydroxylation disequilibrium endmember clumped isotope values. Instead, we see that mixing is non-linear, plotting between a hydroxylation disequilibrium endmember:  $\Delta_{47} = 0.851\text{‰}$ ,  $\delta^{13}\text{C VPDB} = -27.0\text{‰}$  and  $\delta^{18}\text{O VPDB} = -16.7\text{‰}$  [33] and winter (4 °C) and summer (20 °C) equilibrium endmembers for Howden Burn tufas.

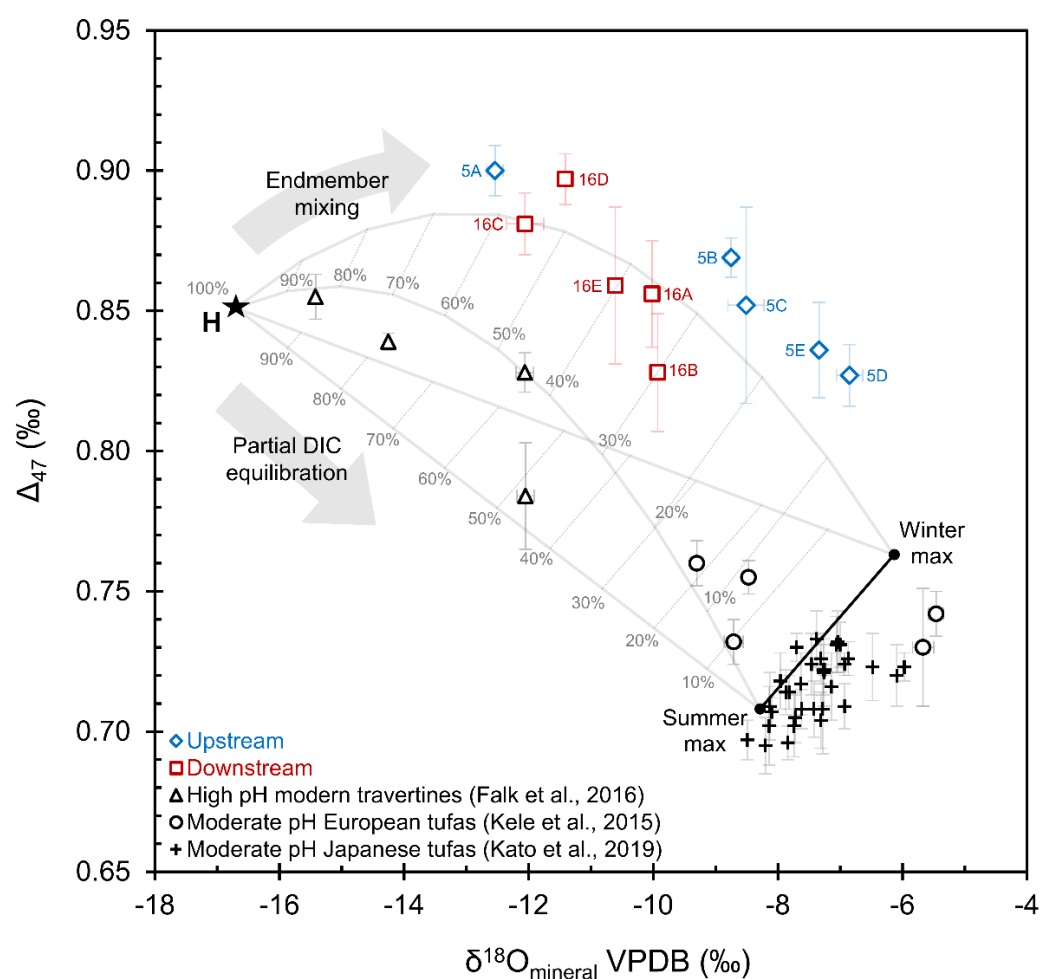


**Figure 4.** Plot of  $\Delta_{47}$  and  $\delta^{18}\text{O}_{\text{mineral}}$  VPDB values for up- and down-stream layers, with data from previous carbonate studies plotted for reference. Disequilibrium hydroxylation (H; black star, from [33]) and seasonal equilibrium endmember values are shown and were used to construct a non-linear mixing zone for DIC endmember mixing in the Howden Burn system. Winter and summer maximum equilibrium values were calculated using water temperature records [53] and regional meteoric rainfall  $\delta^{18}\text{O}$  VSMOW. Grey % values correspond to the ratio of disequilibrium hydroxylation component for any given point on the mixing zone. Linear mixing from DIC equilibration is also shown. Distribution of tufa layer data points between the equilibrium and disequilibrium endmembers corresponds to differing extents of high pH slag leachate dilution from rainfall surface runoff.

This non-linear spread of clumped isotope data is diagnostic of mixing between two distinct DIC endmembers, rather than any partial equilibration of water DIC [86,93]. Variation in apparent clumped isotope disequilibrium along this mixing curve results from changing ratios of the respective endmember components in the final DIC mix, with the largest deviance from a linear mixing trend coming from a 50:50 endmember mix [93]. This mechanism of clumped isotope disequilibrium conforms to field observations regarding rainfall dilution in the Howden Burn, with episodic rainfall dilution of high pH leachate providing the means for mixing of isotopically distinct endmembers.

#### 4.4. Mixing Model Insights

Only half of the tufa layers measured in this study fall within error of the zone of endmember mixing, with the majority of these being from the downstream sample. There are two possible reasons for this; (1) other processes are increasing  $\Delta_{47}$  that are separate from DIC endmember mixing, or (2) endmember values used to construct the non-linear mixing zone shown on Figure 4 are not wholly representative of the Howden Burn carbonate system.

##### 4.4.1. pH Effect

We know from previous studies that precipitation rate is unlikely to have contributed any  $\Delta_{47}$  increase due to the high recorded rates and high pH [5,39,40,53]. However, the speciation effect of high pH is known to produce a  $\Delta_{47}$  reduction of up to 0.050‰ in  $\text{CO}_3^{2-}$  dominated solutions (see Table 1 for  $\text{CO}_3^{2-}$  dominance) [5,39,41]. This offset only reaches its maximum once  $\text{pH} > \sim 12$  [39,41], meaning  $\Delta_{47}$  decrease may not be as much as 0.050‰ in the Howden Burn system, particularly during high rainfall events. If data in this study are corrected for a full pH speciation effect of 0.050‰, this increases  $\Delta_{47}$  further and takes all data points above and out of the non-linear mixing zone in Figure 4. This means pH speciation is not the cause of some data points plotting above the calculated zone of non-linear endmember mixing.

##### 4.4.2. Endmember Suitability

This leaves the question of how representative mixing model endmember values are of the Howden Burn system. Equilibrium  $\Delta_{47}$  calculations use temperature measurements from the Howden Burn and therefore directly correspond to this environment. Despite not being taken as part of this study, the values are sourced from an extensive and long-lasting water temperature archive of the Howden Burn (compiled in [53]) and are therefore deemed to be representative and reliable. Bulk isotope values of the hydroxylation disequilibrium endmember from Falk et al., [33] are near identical to those cited in Dietzel et al. [32], meaning the disequilibrium endmember is also appropriate for modelling this system. That leaves equilibrium  $\delta^{18}\text{O}_{\text{fluid}}$  VSMOW values, which used regional summer and winter  $\delta^{18}\text{O}_{\text{fluid}}$  VSMOW from Keyworth in England [91,92]. These were the most representative data available for the purposes of this study, but given Keyworth is  $\sim 150$  miles south of Consett, these values may differ slightly from the actual  $\delta^{18}\text{O}_{\text{fluid}}$  VSMOW of meteoric rainfall entering the Howden Burn. Further study of the burn hydrochemistry and isotopic measurements of endmember components would be needed to confirm this.

Accurate endmember bulk isotope values for the non-linear mixing model in Figure 4 are important since a relatively small variation can lead to significant differences in the extent of non-linear  $\Delta_{47}$  offset. For example, bulk isotope values differing by 10‰ produce a non-linear mixing effect and  $\Delta_{47}$  increase of up to  $\sim 0.025$ ‰ compared to linear mixing, whereas a difference of 15‰ produces up to  $\sim 0.055$ ‰ increase [8]. Given the underestimation of the model mixing curve relative to tufa isotope data, equilibrium endmember  $\delta^{18}\text{O}_{\text{mineral}}$  VPDB and therefore  $\delta^{18}\text{O}_{\text{fluid}}$  VSMOW would need to be higher if the mixing zone is to cover where all ten tufa layers plot [93].

#### 4.4.3. Correlation with Environmental Conditions

Despite the slight mismatch between non-linear mixing model zone and measured  $\Delta_{47}$  values, the distribution of data points on Figure 4 do provide certain notable trends. Higher upstream  $\delta^{18}\text{O}_{\text{mineral}}$  VPDB values (apart from data point 5A) suggest upstream tufa layers correspond closer to winter temperature and/or water chemistry conditions, relative to downstream layers. One possible environmental explanation for this could be that during winter months increased rainfall and surface runoff dilution of leachate limits the extent of high pH carbonate precipitation to upstream areas. In the drier summer months, dilution is reduced, and  $\text{CO}_2$  hydroxylation-related precipitation takes place further downstream. As a result, downstream carbonates preferentially record summer conditions relative to upstream deposits. However, it is important to acknowledge that the sample size presented here is relatively small. To quantitatively test if this phenomenon is genuine a larger sample size of tufa taken across various period of a seasonal year would be needed, along with accompanying water chemistry data.

Another notable observation from Figure 4 is that the majority of tufa layers plot closer to equilibrium endmembers, suggesting they have a majority equilibrium (i.e., not hydroxylation) component. This is perhaps unexpected given the recorded dominance of hydroxide in this environment (Table 1), but is likely a consequence of the complex control of rainfall in the Howden Burn system. The dilution effect of surface runoff previously discussed lowers stream water pH, reducing the capacity for  $\text{CO}_2$  hydroxylation to occur. At the same time, higher stream discharge increases the precipitation rate of carbonate minerals such as calcite [75,76,104], increasing the volume of carbonate forming during these high rainfall, high flow and lower pH periods. This complexity highlights the importance of understanding and quantifying the controls on carbonate precipitation for interpreting trends in clumped isotope data.

#### 4.5. Quantifying $\Delta_{47}$ Enrichment

Modelling studies of Defliese and Lohmann [93] and more recently Guo [6] suggest the majority of clumped isotope disequilibrium from kinetic processes such as  $\text{CO}_2$  hydroxylation results from non-linear mixing effects rather than any intrinsic fractionation of  $\Delta_{47}$ . Without a more accurate characterization of Howden Burn DIC endmember components it is not possible to quantitatively conclude whether this is the case for data in this study. Compared to linear  $\Delta_{47}$  mixing, clumped isotope values in this study are between  $\sim 0.010\text{‰}$  (16B) and  $\sim 0.145\text{‰}$  (5B) higher than winter and summer linear mixing profiles respectively (see Figure 4). Given bulk isotope endmembers differ by  $27\text{‰}$  for  $\delta^{13}\text{C}$  VPDB and  $8\text{‰}$ – $10\text{‰}$  for  $\delta^{18}\text{O}$  VPDB, these results comparable to the modelling work of Defliese and Lohmann [93], which predict a  $\sim 0.050\text{‰}$  increase in  $\Delta_{47}$  when endmembers differ by  $15\text{‰}$ . The combined effects of this endmember mixing and atmosphere-hydroxide DIC sourcing increases clumped isotope values by  $0.044\text{‰}$ – $0.183\text{‰}$  compared to derived equilibrium values. Given pH speciation is known to reduce clumped isotope values by up to  $0.050\text{‰}$  in  $\text{CO}_3^{2-}$  dominated solutions, overall  $\Delta_{47}$  enrichment could be as high as  $0.233\text{‰}$ . This extent of clumped isotope enrichment bares close resemblance to that recorded in Oman hyperalkaline carbonates, despite the differing climates and water temperatures of the two environments [33].

#### 4.6. Significance and Future Work

This study provides the first clumped isotope data from anthropogenic carbonates, adding to the small number of high pH, non-equilibrium carbonate datasets recorded in the carbonate archive. The heterogeneity of tufa layer isotope values demonstrates that there are multiple competing processes controlling carbonate isotope values in high pH, riverine carbonate systems. The magnitude of clumped isotope disequilibrium and diagnostic trends present in  $\Delta_{47}$  data demonstrates the potential of using anthropogenic car-

bonates to better understand the impact of kinetic effects on clumped isotope values. Future studies could analyze larger numbers of individual carbonate layers from multiple sites (i.e., >2) across the anthropogenic system. These investigations should be concurrent with monitoring of mineral precipitation rates and the accompanying hydrochemical conditions (e.g., real-time rainfall, stream discharge, temperature, water  $\delta^{18}\text{O}$ ) over a full seasonal year. This will quantitatively test which of the environmental variables discussed in this submission (e.g., rainfall, pH, etc.) are the cause and dominant control of clumped isotope disequilibrium variation. Future work should also determine factors such as the organic matter content of carbonates and the consistency of isotope equilibrium endmember signatures.

## 5. Conclusions

The aim of this study was to investigate the clumped isotope values recorded in anthropogenic tufas and test these human-derived carbonates as an archive for evaluating the impact of kinetic fractionations on  $\Delta_{47}$ . We found that, as expected, carbonate clumped isotope values do not correspond to mineral precipitation temperatures and instead record enrichments of +0.044‰–0.183‰ relative to expected equilibrium values. This range includes a negative  $\Delta_{47}$  offset of up to 0.050‰ from the pH speciation effect of  $\text{CO}_3^{2-}$  dominated solutions, meaning hydroxylation-related  $\Delta_{47}$  enrichment could be as high as 0.233‰. Non-linear distribution of clumped isotope data indicates DIC endmember mixing is responsible for variable extents of disequilibrium, rather than partial equilibration of DIC. Episodic dilution of hydroxide-rich stream waters by equilibrated rainfall surface runoff provides a plausible mechanism for endmember mixing in this environment.

Increases of ~0.010‰–0.145‰ in  $\Delta_{47}$  values relative to linear summer and winter mixing profiles indicates that the majority of increase in clumped isotope values results from a combination of non-linear mixing effects and atmosphere-hydroxide sourcing of DIC. Through time, tufa layers inherit clumped isotope signatures that correspond to the mixing of disequilibrium ( $\text{CO}_2$  hydroxylation) and equilibrium (surface runoff) endmembers. Layers that form during high rainfall (i.e., high dilution, lower pH) events are expected to record bulk and clumped isotope values closer to expected equilibrium values than those forming during low rainfall (i.e., low dilution, high pH) periods.

The diagnostic trends and variation in clumped isotope values present in this small dataset demonstrates the potential of anthropogenic carbonate systems as a useful archive for studying and quantifying kinetic effects in clumped isotopes.

**Supplementary Materials:** The following supporting information can be downloaded at: <https://www.mdpi.com/article/10.3390/min12121611/s1>; Figure S1: 1880 map showing the original, pre-steelworks profile of the Howden Burn. Figure S2: 1890 map showing the initial infilling of the Howden Burn profile. Figure S3: 1920 map showing the infilling of the Howden Burn after 30 years of production. Figure S4: 1930 map showing slag deposition reaching Pemberton Road. Figure S5: 1960 map showing some re-profiling of the Burn under Pemberton Road. Figure S6: 1945 aerial photograph captures the extent of slag deposition in the Howden Burn profile. Figure S7: Present day aerial view of Howden Burn and now-vegetated Conssett heaps. Figure S8: Picture of upstream Howden Burn tufa hand specimen CHS5. Figure S9: Picture of downstream Howden Burn tufa hand specimen CHS16.

**Author Contributions:** Conceptualization, C.H. and J.M.; methodology, C.H. and J.M.; software, C.J.; validation, C.J.; formal analysis, C.H. and C.J.; investigation, C.H.; resources, C.H. and J.M.; data curation, C.H. and C.J.; writing—original draft preparation, C.H.; writing—review and editing, C.H., J.M., and C.J.; visualization, C.H. and J.M.; supervision, C.H. and J.M.; project administration, C.H. and J.M.; funding acquisition, C.H. and J.M. All authors have read and agreed to the published version of the manuscript.

**Funding:** C.H. was funded by an Angus Mitchell research scholarship and a Sir Alwyn Williams postgraduate research award, both from the University of Glasgow. J.M. acknowledges funding from the SAGES+ Small Grant Scheme for the clumped isotope analysis.

**Data Availability Statement:** The data presented in this study are openly available in the British Geological Survey (BGS) National Geoscience Data Centre (NGDC) at [89].

**Acknowledgments:** We would like to thank Editor and the three anonymous reviewers for their guidance and constructive suggestions that helped improve the manuscript. Will Mayes is thanked for showing the authors around the field site and for many fruitful discussions during the work. The late Paul Younger is thanked for introducing J.M. to Consett, anthropogenic tufas, and steel slags more generally.

**Conflicts of Interest:** The authors declare no conflicts of interest. The funders had no role in the design of the study; in the collection, analyses, or interpretation of data; in the writing of the manuscript; or in the decision to publish the results.

## References

1. Ghosh, P.; Adkins, J.; Affek, H.; Balta, B.; Guo, W.; Schauble, E.A.; Schrag, D.; Eiler, J.M.  $^{13}\text{C}$ – $^{18}\text{O}$  Bonds in Carbonate Minerals: A New Kind of Paleothermometer. *Geochim. Cosmochim. Acta* **2006**, *70*, 1439–1456. <https://doi.org/10.1016/j.gca.2005.11.014>.
2. Schauble, E.A.; Ghosh, P.; Eiler, J.M. Preferential Formation of  $^{13}\text{C}$ – $^{18}\text{O}$  Bonds in Carbonate Minerals, Estimated Using First-Principles Lattice Dynamics. *Geochim. Cosmochim. Acta* **2006**, *70*, 2510–2529. <https://doi.org/10.1016/j.gca.2006.02.011>.
3. Eiler, J.M. “Clumped-Isotope” Geochemistry—The Study of Naturally-Occurring, Multiply-Substituted Isotopologues. *Earth Planet. Sci. Lett.* **2007**, *262*, 309–327. <https://doi.org/10.1016/j.epsl.2007.08.020>.
4. Guo, W.; Mosenfelder, J.L.; Goddard, W.A.; Eiler, J.M. Isotopic Fractionations Associated with Phosphoric Acid Digestion of Carbonate Minerals: Insights from First-Principles Theoretical Modeling and Clumped Isotope Measurements. *Geochim. Cosmochim. Acta* **2009**, *73*, 7203–7225. <https://doi.org/10.1016/j.gca.2009.05.071>.
5. Kluge, T.; John, C.M.; Boch, R.; Kele, S. Assessment of Factors Controlling Clumped Isotopes and  $\delta^{18}\text{O}$  Values of Hydrothermal Vent Calcites. *Geochem. Geophys. Geosyst.* **2018**, *19*, 1844–1858. <https://doi.org/10.1029/2017GC006969>.
6. Guo, W. Kinetic Clumped Isotope Fractionation in the DIC–H<sub>2</sub>O–CO<sub>2</sub> System: Patterns, Controls, and Implications. *Geochim. Cosmochim. Acta* **2020**, *268*, 230–257. <https://doi.org/10.1016/j.gca.2019.07.055>.
7. Zaarur, S.; Affek, H.P.; Brandon, M.T. A Revised Calibration of the Clumped Isotope Thermometer. *Earth Planet. Sci. Lett.* **2013**, *382*, 47–57. <https://doi.org/10.1016/j.epsl.2013.07.026>.
8. Defliese, W.F.; Hren, M.T.; Lohmann, K.C. Compositional and Temperature Effects of Phosphoric Acid Fractionation on  $\Delta_{47}$  Analysis and Implications for Discrepant Calibrations. *Chem. Geol.* **2015**, *396*, 51–60. <https://doi.org/10.1016/j.chemgeo.2014.12.018>.
9. Kluge, T.; John, C.M.; Jourdan, A.-L.; Davis, S.; Crawshaw, J. Laboratory Calibration of the Calcium Carbonate Clumped Isotope Thermometer in the 25–250°C Temperature Range. *Geochim. Cosmochim. Acta* **2015**, *157*, 213–227. <https://doi.org/10.1016/j.gca.2015.02.028>.
10. Kele, S.; Breitenbach, S.F.M.; Capezzuoli, E.; Meckler, A.N.; Ziegler, M.; Millan, I.M.; Kluge, T.; Deák, J.; Hanselmann, K.; John, C.M.; et al. Temperature Dependence of Oxygen- and Clumped Isotope Fractionation in Carbonates: A Study of Travertines and Tufas in the 6–95°C Temperature Range. *Geochim. Cosmochim. Acta* **2015**, *168*, 172–192. <https://doi.org/10.1016/j.gca.2015.06.032>.
11. Kelson, J.R.; Huntington, K.W.; Schauer, A.J.; Saenger, C.; Lechler, A.R. Toward a Universal Carbonate Clumped Isotope Calibration: Diverse Synthesis and Preparatory Methods Suggest a Single Temperature Relationship. *Geochim. Cosmochim. Acta* **2017**, *197*, 104–131. <https://doi.org/10.1016/j.gca.2016.10.010>.
12. Bonifacie, M.; Calmels, D.; Eiler, J.M.; Horita, J.; Chaduteau, C.; Vasconcelos, C.; Agrinier, P.; Katz, A.; Passey, B.H.; Ferry, J.M.; et al. Calibration of the Dolomite Clumped Isotope Thermometer from 25 to 350 °C, and Implications for a Universal Calibration for All (Ca, Mg, Fe)CO<sub>3</sub> Carbonates. *Geochim. Cosmochim. Acta* **2017**, *200*, 255–279. <https://doi.org/10.1016/j.gca.2016.11.028>.
13. Petersen, S.V.; Defliese, W.F.; Saenger, C.; Daëron, M.; Huntington, K.W.; John, C.M.; Kelson, J.R.; Bernasconi, S.M.; Colman, A.S.; Kluge, T.; et al. Effects of Improved  $^{17}\text{O}$  Correction on Interlaboratory Agreement in Clumped Isotope Calibrations, Estimates of Mineral-Specific Offsets, and Temperature Dependence of Acid Digestion Fractionation. *Geochem. Geophys. Geosyst.* **2019**, *20*, 3495–3519. <https://doi.org/10.1029/2018GC008127>.
14. Davies, A.J.; John, C.M. The Clumped ( $^{13}\text{C}$  $^{18}\text{O}$ ) Isotope Composition of Echinoid Calcite: Further Evidence for “Vital Effects” in the Clumped Isotope Proxy. *Geochim. Cosmochim. Acta* **2019**, *245*, 172–189. <https://doi.org/10.1016/j.gca.2018.07.038>.
15. Affek, H.P.; Bar-Matthews, M.; Ayalon, A.; Matthews, A.; Eiler, J.M. Glacial/Interglacial Temperature Variations in Soreq Cave Speleothems as Recorded by ‘Clumped Isotope’ Thermometry. *Geochim. Cosmochim. Acta* **2008**, *72*, 5351–5360. <https://doi.org/10.1016/j.gca.2008.06.031>.
16. Kluge, T.; Affek, H.P.; Zhang, Y.G.; Dublyansky, Y.; Spötl, C.; Immenhauser, A.; Richter, D.K. Clumped Isotope Thermometry of Cryogenic Cave Carbonates. *Geochim. Cosmochim. Acta* **2014**, *126*, 541–554. <https://doi.org/10.1016/j.gca.2013.11.011>.
17. Henkes, G.A.; Passey, B.H.; Grossman, E.L.; Shenton, B.J.; Pérez-Huerta, A.; Yancey, T.E. Temperature Limits for Preservation of Primary Calcite Clumped Isotope Paleotemperatures. *Geochim. Cosmochim. Acta* **2014**, *139*, 362–382. <https://doi.org/10.1016/j.gca.2014.04.040>.

18. Rodríguez-Sanz, L.; Bernasconi, S.M.; Marino, G.; Heslop, D.; Müller, I.A.; Fernandez, A.; Grant, K.M.; Rohling, E.J. Penultimate Deglacial Warming across the Mediterranean Sea Revealed by Clumped Isotopes in Foraminifera. *Sci. Rep.* **2017**, *7*, 16572. <https://doi.org/10.1038/s41598-017-16528-6>.
19. Evans, D.; Sagoo, N.; Renema, W.; Cotton, L.J.; Müller, W.; Todd, J.A.; Saraswati, P.K.; Stassen, P.; Ziegler, M.; Pearson, P.N.; et al. Eocene Greenhouse Climate Revealed by Coupled Clumped Isotope-Mg/Ca Thermometry. *Proc. Natl. Acad. Sci. USA* **2018**, *115*, 1174–1179. <https://doi.org/10.1073/pnas.1714744115>.
20. Henkes, G.A.; Passey, B.H.; Grossman, E.L.; Shenton, B.J.; Yancey, T.E.; Pérez-Huerta, A. Temperature Evolution and the Oxygen Isotope Composition of Phanerozoic Oceans from Carbonate Clumped Isotope Thermometry. *Earth Planet. Sci. Lett.* **2018**, *490*, 40–50. <https://doi.org/10.1016/j.epsl.2018.02.001>.
21. Dale, A.; John, C.M.; Mozley, P.S.; Smalley, P.C.; Muggeridge, A.H. Time-Capsule Concretions: Unlocking Burial Diagenetic Processes in the Mancos Shale Using Carbonate Clumped Isotopes. *Earth Planet. Sci. Lett.* **2014**, *394*, 30–37. <https://doi.org/10.1016/j.epsl.2014.03.004>.
22. Shenton, B.J.; Grossman, E.L.; Passey, B.H.; Henkes, G.A.; Becker, T.P.; Laya, J.C.; Perez-Huerta, A.; Becker, S.P.; Lawson, M. Clumped Isotope Thermometry in Deeply Buried Sedimentary Carbonates: The Effects of Bond Reordering and Recrystallization. *Geol. Soc. Am. Bull.* **2015**, *127*, B31169.1. <https://doi.org/10.1130/B31169.1>.
23. MacDonald, J.M.; John, C.M.; Girard, J.-P. Testing Clumped Isotopes as a Reservoir Characterization Tool: A Comparison with Fluid Inclusions in a Dolomitized Sedimentary Carbonate Reservoir Buried to 2–4 Km. *Geol. Soc. Lond. Spec. Publ.* **2018**, *468*, 189–202. <https://doi.org/10.1144/SP468.7>.
24. Lawson, M.; Shenton, B.J.; Stolper, D.A.; Eiler, J.M.; Rasbury, E.T.; Becker, T.P.; Phillips-Lander, C.M.; Buono, A.S.; Becker, S.P.; Pottorf, R.; et al. Deciphering the Diagenetic History of the El Abra Formation of Eastern Mexico Using Reordered Clumped Isotope Temperatures and U-Pb Dating. *GSA Bull.* **2018**, *130*, 617–629. <https://doi.org/10.1130/B31656.1>.
25. Pagel, M.; Bonifacie, M.; Schneider, D.A.; Gautheron, C.; Brigaud, B.; Calmels, D.; Cros, A.; Saint-Bezar, B.; Landrein, P.; Sutcliffe, C.; et al. Improving Paleohydrological and Diagenetic Reconstructions in Calcite Veins and Breccia of a Sedimentary Basin by Combining  $\Delta_{47}$  Temperature,  $\delta^{18}\text{O}_{\text{water}}$  and U-Pb Age. *Chem. Geol.* **2018**, *481*, 1–17. <https://doi.org/10.1016/j.chemgeo.2017.12.026>.
26. Millán, M.I.; Machel, H.; Bernasconi, S.M. Constraining Temperatures of Formation and Composition of Dolomitizing Fluids In the Upper Devonian Nisku Formation (Alberta, Canada) With Clumped Isotopes. *J. Sediment. Res.* **2016**, *86*, 107–112. <https://doi.org/10.2110/jsr.2016.6>.
27. Manganot, X.; Gasparrini, M.; Rouchon, V.; Bonifacie, M. Basin-Scale Thermal and Fluid Flow Histories Revealed by Carbonate Clumped Isotopes ( $\Delta_{47}$ )—Middle Jurassic Carbonates of the Paris Basin Depocentre. *Sedimentology* **2018**, *65*, 123–150. <https://doi.org/10.1111/sed.12427>.
28. MacDonald, J.M.; Faithful, J.W.; Roberts, N.M.W.; Davies, A.J.; Holdsworth, C.M.; Newton, M.; Williamson, S.; Boyce, A.; John, C.M. Clumped-Isotope Palaeothermometry and LA-ICP-MS U-Pb Dating of Lava-Pile Hydrothermal Calcite Veins. *Contrib. Mineral. Petrol.* **2019**, *174*, 63. <https://doi.org/10.1007/s00410-019-1599-x>.
29. Barnes, I.; O’Neil, J.R. Calcium-Magnesium Carbonate Solid Solutions from Holocene Conglomerate Cements and Travertines in the Coast Range of California. *Geochim. Cosmochim. Acta* **1971**, *35*, 699–718. [https://doi.org/10.1016/0016-7037\(71\)90068-8](https://doi.org/10.1016/0016-7037(71)90068-8).
30. Barnes, I.; O’Neil, J.R. The Relationship between Fluids in Some Fresh Alpine-Type Ultramafics and Possible Modern Serpentinization, Western United States. *GSA Bull.* **1969**, *80*, 1947–1960. [https://doi.org/10.1130/0016-7606\(1969\)80\[1947:TRBFIS\]2.0.CO;2](https://doi.org/10.1130/0016-7606(1969)80[1947:TRBFIS]2.0.CO;2).
31. Clark, I.D.; Fontes, J.-C.; Fritz, P. Stable Isotope Disequilibria in Travertine from High PH Waters: Laboratory Investigations and Field Observations from Oman. *Geochim. Cosmochim. Acta* **1992**, *56*, 2041–2050. [https://doi.org/10.1016/0016-7037\(92\)90328-G](https://doi.org/10.1016/0016-7037(92)90328-G).
32. Dietzel, M.; Usdowski, E.; Hoefs, J. Chemical and  $^{13}\text{C}/^{12}\text{C}$ - and  $^{18}\text{O}/^{16}\text{O}$ -Isotope Evolution of Alkaline Drainage Waters and the Precipitation of Calcite. *Appl. Geochem.* **1992**, *7*, 177–184. [https://doi.org/10.1016/0883-2927\(92\)90035-2](https://doi.org/10.1016/0883-2927(92)90035-2).
33. Falk, E.S.; Guo, W.; Paukert, A.N.; Matter, J.M.; Mervine, E.M.; Kelemen, P.B. Controls on the Stable Isotope Compositions of Travertine from Hyperalkaline Springs in Oman: Insights from Clumped Isotope Measurements. *Geochim. Cosmochim. Acta* **2016**, *192*, 1–28. <https://doi.org/10.1016/j.gca.2016.06.026>.
34. O’Neil, J.R.; Barnes, I.  $\text{C}^{13}$  and  $\text{O}^{18}$  Compositions in Some Fresh-Water Carbonates Associated with Ultramafic Rocks and Serpentinites: Western United States. *Geochim. Cosmochim. Acta* **1971**, *35*, 687–697. [https://doi.org/10.1016/0016-7037\(71\)90067-6](https://doi.org/10.1016/0016-7037(71)90067-6).
35. Burgener, L.K.; Huntington, K.W.; Sletten, R.; Watkins, J.M.; Quade, J.; Hallet, B. Clumped Isotope Constraints on Equilibrium Carbonate Formation and Kinetic Isotope Effects in Freezing Soils. *Geochim. Cosmochim. Acta* **2018**, *235*, 402–430. <https://doi.org/10.1016/j.gca.2018.06.006>.
36. Clark, I.D.; Lauriol, B. Kinetic Enrichment of Stable Isotopes in Cryogenic Calcites. *Chem. Geol.* **1992**, *102*, 217–228. [https://doi.org/10.1016/0009-2541\(92\)90157-Z](https://doi.org/10.1016/0009-2541(92)90157-Z).
37. Friedman, I. Some Investigations of the Deposition of Travertine from Hot Springs—I. The Isotopic Chemistry of a Travertine-Depositing Spring. *Geochim. Cosmochim. Acta* **1970**, *34*, 1303–1315. [https://doi.org/10.1016/0016-7037\(70\)90043-8](https://doi.org/10.1016/0016-7037(70)90043-8).
38. Loyd, S.J.; Sample, J.; Tripathi, R.E.; Defliese, W.F.; Brooks, K.; Hovland, M.; Torres, M.; Marlow, J.; Hancock, L.G.; Martin, R.; et al. Methane Seep Carbonates Yield Clumped Isotope Signatures out of Equilibrium with Formation Temperatures. *Nat. Commun.* **2016**, *7*, 12274. <https://doi.org/10.1038/ncomms12274>.

39. Tripathi, A.K.; Hill, P.S.; Eagle, R.A.; Mosenfelder, J.L.; Tang, J.; Schauble, E.A.; Eiler, J.M.; Zeebe, R.E.; Uchikawa, J.; Coplen, T.B.; et al. Beyond Temperature: Clumped Isotope Signatures in Dissolved Inorganic Carbon Species and the Influence of Solution Chemistry on Carbonate Mineral Composition. *Geochim. Cosmochim. Acta* **2015**, *166*, 344–371. <https://doi.org/10.1016/j.gca.2015.06.021>.
40. Watkins, J.M.; Hunt, J.D. A Process-Based Model for Non-Equilibrium Clumped Isotope Effects in Carbonates. *Earth Planet. Sci. Lett.* **2015**, *432*, 152–165. <https://doi.org/10.1016/j.epsl.2015.09.042>.
41. Hill, P.S.; Tripathi, A.K.; Schauble, E.A. Theoretical Constraints on the Effects of PH, Salinity, and Temperature on Clumped Isotope Signatures of Dissolved Inorganic Carbon Species and Precipitating Carbonate Minerals. *Geochim. Cosmochim. Acta* **2014**, *125*, 610–652. <https://doi.org/10.1016/j.gca.2013.06.018>.
42. Tang, J.; Dietzel, M.; Fernandez, A.; Tripathi, A.K.; Rosenheim, B.E. Evaluation of Kinetic Effects on Clumped Isotope Fractionation ( $\Delta_{47}$ ) during Inorganic Calcite Precipitation. *Geochim. Cosmochim. Acta* **2014**, *134*, 120–136. <https://doi.org/10.1016/j.gca.2014.03.005>.
43. McConnaughey, T.  $^{13}\text{C}$  and  $^{18}\text{O}$  Isotopic Disequilibrium in Biological Carbonates: I. Patterns. *Geochim. Cosmochim. Acta* **1989**, *53*, 151–162. [https://doi.org/10.1016/0016-7037\(89\)90282-2](https://doi.org/10.1016/0016-7037(89)90282-2).
44. McConnaughey, T.  $^{13}\text{C}$  and  $^{18}\text{O}$  Isotopic Disequilibrium in Biological Carbonates: II. In Vitro Simulation of Kinetic Isotope Effects. *Geochim. Cosmochim. Acta* **1989**, *53*, 163–171. [https://doi.org/10.1016/0016-7037\(89\)90283-4](https://doi.org/10.1016/0016-7037(89)90283-4).
45. Wilson, S.A.; Barker, S.L.L.; Dipple, G.M.; Atudorei, V. Isotopic Disequilibrium during Uptake of Atmospheric  $\text{CO}_2$  into Mine Process Waters: Implications for  $\text{CO}_2$  Sequestration. *Environ. Sci. Technol.* **2010**, *44*, 9522–9529. <https://doi.org/10.1021/es1021125>.
46. Bajnai, D.; Guo, W.; Spötl, C.; Coplen, T.B.; Methner, K.; Löffler, N.; Krsnik, E.; Gischler, E.; Hansen, M.; Henkel, D.; et al. Dual Clumped Isotope Thermometry Resolves Kinetic Biases in Carbonate Formation Temperatures. *Nat. Commun.* **2020**, *11*, 4005. <https://doi.org/10.1038/s41467-020-17501-0>.
47. Guo, W.; Zhou, C. Patterns and Controls of Disequilibrium Isotope Effects in Speleothems: Insights from an Isotope-Enabled Diffusion-Reaction Model and Implications for Quantitative Thermometry. *Geochim. Cosmochim. Acta* **2019**, *267*, 196–226. <https://doi.org/10.1016/j.gca.2019.07.028>.
48. Mills, G.A.; Urey, H.C. The Kinetics of Isotopic Exchange between Carbon Dioxide, Bicarbonate Ion, Carbonate Ion and Water. *J. Am. Chem. Soc.* **1940**, *62*, 1019–1026. <https://doi.org/10.1021/ja01862a010>.
49. Pinsent, B.R.W.; Pearson, L.; Roughton, F.J.W. The Kinetics of Combination of Carbon Dioxide with Hydroxide Ions. *Trans. Faraday Soc.* **1956**, *52*, 1512. <https://doi.org/10.1039/tf9565201512>.
50. Turner, J.V. Kinetic Fractionation of Carbon-13 during Calcium Carbonate Precipitation. *Geochim. Cosmochim. Acta* **1982**, *46*, 1183–1191. [https://doi.org/10.1016/0016-7037\(82\)90004-7](https://doi.org/10.1016/0016-7037(82)90004-7).
51. Usdowski, E.; Hoefs, J.  $^{13}\text{C}/^{12}\text{C}$  Partitioning and Kinetics of  $\text{CO}_2$  Absorption by Hydroxide Buffer Solutions. *Earth Planet. Sci. Lett.* **1986**, *80*, 130–134. [https://doi.org/10.1016/0012-821X\(86\)90025-7](https://doi.org/10.1016/0012-821X(86)90025-7).
52. Renforth, P.; Manning, D.A.C.; Lopez-Capel, E. Carbonate Precipitation in Artificial Soils as a Sink for Atmospheric Carbon Dioxide. *Appl. Geochem.* **2009**, *24*, 1757–1764. <https://doi.org/10.1016/j.apgeochem.2009.05.005>.
53. Mayes, W.M.; Riley, A.L.; Gomes, H.I.; Brabham, P.; Hamlyn, J.; Pullin, H.; Renforth, P. Atmospheric  $\text{CO}_2$  Sequestration in Iron and Steel Slag: Consett, County Durham, United Kingdom. *Environ. Sci. Technol.* **2018**, *52*, 7892–7900. <https://doi.org/10.1021/acs.est.8b01883>.
54. Kelemen, P.B.; Matter, J. In Situ Carbonation of Peridotite for  $\text{CO}_2$  Storage. *Proc. Natl. Acad. Sci. USA* **2008**, *105*, 17295–17300.
55. Rodríguez-Berriguete, Á.; Alonso-Zarza, A.M.; Martín-García, R.; Cabrera, M.d.C. Sedimentology and Geochemistry of a Human-Induced Tufa Deposit: Implications for Palaeoclimatic Research. *Sedimentology* **2018**, *65*, 2253–2277. <https://doi.org/10.1111/sed.12464>.
56. Andrews, J.E.; Gare, S.G.; Dennis, P.F. Unusual Isotopic Phenomena in Welsh Quarry Water and Carbonate Crusts. *Terra Nova* **1997**, *9*, 67–70. <https://doi.org/10.1111/j.1365-3121.1997.tb00004.x>.
57. Moyce, E.B.A.; Milodowski, A.E.; Morris, K.; Shaw, S. Herbert’s Quarry, South Wales—An Analogue for Host-Rock Alteration at a Cementitious Radioactive Waste Repository? *Mineral. Mag.* **2015**, *79*, 1407–1418. <https://doi.org/10.1180/minmag.2015.079.6.16>.
58. Ettler, V.; Zelená, O.; Mihaljevič, M.; Šebek, O.; Strnad, L.; Coufal, P.; Bezdička, P. Removal of Trace Elements from Landfill Leachate by Calcite Precipitation. *J. Geochem. Explor.* **2006**, *88*, 28–31. <https://doi.org/10.1016/j.gexplo.2005.08.010>.
59. Manning, D.A.C. Calcite Precipitation in Landfills: An Essential Product of Waste Stabilization. *Mineral. Mag.* **2001**, *65*, 603–610. <https://doi.org/10.1180/002646101317018424>.
60. Bayless, E.R.; Schulz, M.S. Mineral Precipitation and Dissolution at Two Slag-Disposal Sites in Northwestern Indiana, USA. *Environ. Geol.* **2003**, *45*, 252–261. <https://doi.org/10.1007/s00254-003-0875-1>.
61. Roadcap, G.S.; Kelly, W.R.; Bethke, C.M. Geochemistry of Extremely Alkaline (PH > 12) Ground Water in Slag-Fill Aquifers. *Groundwater* **2005**, *43*, 806–816. <https://doi.org/10.1111/j.1745-6584.2005.00060.x>.
62. Huijgen, W.J.J.; Comans, R.N.J. Carbonation of Steel Slag for  $\text{CO}_2$  Sequestration: Leaching of Products and Reaction Mechanisms. *Environ. Sci. Technol.* **2006**, *40*, 2790–2796. <https://doi.org/10.1021/es052534b>.
63. Mayes, W.M.; Younger, P.L.; Aumônier, J. Hydrogeochemistry of Alkaline Steel Slag Leachates in the UK. *Water Air Soil Pollut.* **2008**, *195*, 35–50. <https://doi.org/10.1007/s11270-008-9725-9>.
64. Hall, C.; Large, D.J.; Adderley, B.; West, H.M. Calcium Leaching from Waste Steelmaking Slag: Significance of Leachate Chemistry and Effects on Slag Grain Mineralogy. *Miner. Eng.* **2014**, *65*, 156–162. <https://doi.org/10.1016/j.mineng.2014.06.002>.

65. Riley, A.L.; Mayes, W.M. Long-Term Evolution of Highly Alkaline Steel Slag Drainage Waters. *Environ. Monit. Assess.* **2015**, *187*, 463. <https://doi.org/10.1007/s10661-015-4693-1>.
66. Washbourne, C.-L.; Lopez-Capel, E.; Renforth, P.; Ascough, P.L.; Manning, D.A.C. Rapid Removal of Atmospheric CO<sub>2</sub> by Urban Soils. *Environ. Sci. Technol.* **2015**, *49*, 5434–5440. <https://doi.org/10.1021/es505476d>.
67. Washbourne, C.-L.; Renforth, P.; Manning, D.A.C. Investigating Carbonate Formation in Urban Soils as a Method for Capture and Storage of Atmospheric Carbon. *Sci. Total Environ.* **2012**, *431*, 166–175. <https://doi.org/10.1016/j.scitotenv.2012.05.037>.
68. Moyce, E.B.A.; Rochelle, C.; Morris, K.; Milodowski, A.E.; Chen, X.; Thornton, S.; Small, J.S.; Shaw, S. Rock Alteration in Alkaline Cement Waters over 15 Years and Its Relevance to the Geological Disposal of Nuclear Waste. *Appl. Geochem.* **2014**, *50*, 91–105. <https://doi.org/10.1016/j.apgeochem.2014.08.003>.
69. Martin, L.H.J.; Leemann, A.; Milodowski, A.E.; Mäder, U.K.; Münch, B.; Giroud, N. A Natural Cement Analogue Study to Understand the Long-Term Behaviour of Cements in Nuclear Waste Repositories: Maqarin (Jordan). *Appl. Geochem.* **2016**, *71*, 20–34. <https://doi.org/10.1016/j.apgeochem.2016.05.009>.
70. Brocken, H.; Nijland, T.G. White Efflorescence on Brick Masonry and Concrete Masonry Blocks, with Special Emphasis on Sulfate Efflorescence on Concrete Blocks. *Constr. Build. Mater.* **2004**, *18*, 315–323. <https://doi.org/10.1016/j.conbuildmat.2004.02.004>.
71. Macleod, G.; Fallick, A.E.; Hall, A.J. The Mechanism of Carbonate Growth on Concrete Structures, as Elucidated by Carbon and Oxygen Isotope Analyses. *Chem. Geol. Isot. Geosci. Sect.* **1991**, *86*, 335–343. [https://doi.org/10.1016/0168-9622\(91\)90015-O](https://doi.org/10.1016/0168-9622(91)90015-O).
72. Hull, S.L.; Oty, U.V.; Mayes, W.M. Rapid Recovery of Benthic Invertebrates Downstream of Hyperalkaline Steel Slag Discharges. *Hydrobiologia* **2014**, *736*, 83–97. <https://doi.org/10.1007/s10750-014-1894-5>.
73. Harber, A.J.; Forth, R.A. The Contamination of Former Iron and Steel Works Sites. *Environ. Geol.* **2001**, *40*, 324–330. <https://doi.org/10.1007/s002540000167>.
74. Ford, T.D.; Pedley, H.M. A Review of Tufa and Travertine Deposits of the World. *Earth-Sci. Rev.* **1996**, *41*, 117–175. [https://doi.org/10.1016/S0012-8252\(96\)00030-X](https://doi.org/10.1016/S0012-8252(96)00030-X).
75. Kano, A.; Matsuoka, J.; Kojo, T.; Fujii, H. Origin of Annual Laminations in Tufa Deposits, Southwest Japan. *Palaeogeogr. Palaeoclimatol. Palaeoecol.* **2003**, *191*, 243–262. [https://doi.org/10.1016/0031-0182\(02\)00717-4](https://doi.org/10.1016/0031-0182(02)00717-4).
76. Kawai, T.; Kano, A.; Hori, M. Geochemical and Hydrological Controls on Biannual Lamination of Tufa Deposits. *Sediment. Geol.* **2009**, *213*, 41–50. <https://doi.org/10.1016/j.sedgeo.2008.11.003>.
77. Capezzuoli, E.; Gandin, A.; Pedley, M. Decoding Tufa and Travertine (Fresh Water Carbonates) in the Sedimentary Record: The State of the Art. *Sedimentology* **2014**, *61*, 1–21. <https://doi.org/10.1111/sed.12075>.
78. Adlan, Q.; Davies, A.J.; John, C.M. Effects of Oxygen Plasma Ashing Treatment on Carbonate Clumped Isotopes. *Rapid Commun. Mass Spectrom.* **2020**, *34*, e8802. <https://doi.org/10.1002/rcm.8802>.
79. Huntington, K.W.; Eiler, J.M.; Affek, H.P.; Guo, W.; Bonifacie, M.; Yeung, L.Y.; Thiagarajan, N.; Passey, B.; Tripathi, A.; Daëron, M.; et al. Methods and Limitations of ‘Clumped’ CO<sub>2</sub> Isotope ( $\Delta_{47}$ ) Analysis by Gas-Source Isotope Ratio Mass Spectrometry. *J. Mass Spectrom.* **2009**, *44*, 1318–1329. <https://doi.org/10.1002/jms.1614>.
80. Cruset, D.; Cantarero, I.; Travé, A.; Vergés, J.; John, C.M. Crestal Graben Fluid Evolution during Growth of the Puig-Reig Anticline (South Pyrenean Fold and Thrust Belt). *J. Geodyn.* **2016**, *101*, 30–50. <https://doi.org/10.1016/j.jog.2016.05.004>.
81. Dennis, K.J.; Affek, H.P.; Passey, B.H.; Schrag, D.P.; Eiler, J.M. Defining an Absolute Reference Frame for ‘Clumped’ Isotope Studies of CO<sub>2</sub>. *Geochim. Cosmochim. Acta* **2011**, *75*, 7117–7131. <https://doi.org/10.1016/j.gca.2011.09.025>.
82. John, C.M.; Bowen, D. Community Software for Challenging Isotope Analysis: First Applications of ‘Easotope’ to Clumped Isotopes. *Rapid Commun. Mass Spectrom.* **2016**, *30*, 2285–2300. <https://doi.org/10.1002/rcm.7720>.
83. Bernasconi, S.M.; Hu, B.; Wacker, U.; Fiebig, J.; Breitenbach, S.F.M.; Rutz, T. Background Effects on Faraday Collectors in Gas-Source Mass Spectrometry and Implications for Clumped Isotope Measurements. *Rapid Commun. Mass Spectrom.* **2013**, *27*, 603–612. <https://doi.org/10.1002/rcm.6490>.
84. Meckler, A.N.; Ziegler, M.; Millán, M.I.; Breitenbach, S.F.M.; Bernasconi, S.M. Long-Term Performance of the Kiel Carbonate Device with a New Correction Scheme for Clumped Isotope Measurements. *Rapid Commun. Mass Spectrom.* **2014**, *28*, 1705–1715. <https://doi.org/10.1002/rcm.6949>.
85. Bernasconi, S.M.; Müller, I.A.; Bergmann, K.D.; Breitenbach, S.F.M.; Fernandez, A.; Hodell, D.A.; Jaggi, M.; Meckler, A.N.; Millán, I.; Ziegler, M. Reducing Uncertainties in Carbonate Clumped Isotope Analysis Through Consistent Carbonate-Based Standardization. *Geochem. Geophys. Geosyst.* **2018**, *19*, 2895–2914. <https://doi.org/10.1029/2017GC007385>.
86. Eiler, J.M.; Schauble, E. <sup>18</sup>O<sup>13</sup>C<sup>16</sup>O in Earth’s Atmosphere. *Geochim. Cosmochim. Acta* **2004**, *68*, 4767–4777. <https://doi.org/10.1016/j.gca.2004.05.035>.
87. Guo, W.; Eiler, J.M. Temperatures of Aqueous Alteration and Evidence for Methane Generation on the Parent Bodies of the CM Chondrites. *Geochim. Cosmochim. Acta* **2007**, *71*, 5565–5575. <https://doi.org/10.1016/j.gca.2007.07.029>.
88. Brand, W.A.; Assonov, S.S.; Coplen, T.B. Correction for the <sup>17</sup>O Interference in  $\delta^{13}\text{C}$  Measurements When Analyzing CO<sub>2</sub> with Stable Isotope Mass Spectrometry (IUPAC Technical Report). *Pure Appl. Chem.* **2010**, *82*, 1719–1733. <https://doi.org/10.1351/PAC-REP-09-01-05>.
89. Holdsworth, C.; MacDonald, J.; John, C. **2022**. Clumped isotope data from high-pH anthropogenic tufa in the Howden Burn, Consett, North East England; NERC EDS National Geoscience Data Centre; <https://doi.org/10.5285/61ec053d-b8f9-4ec7-8d98-8423bf253bef>

90. Kim, S.-T.; O'Neil, J.R. Equilibrium and Nonequilibrium Oxygen Isotope Effects in Synthetic Carbonates. *Geochim. Cosmochim. Acta* **1997**, *61*, 3461–3475. [https://doi.org/10.1016/S0016-7037\(97\)00169-5](https://doi.org/10.1016/S0016-7037(97)00169-5).
91. Darling, W.G.; Bath, A.H.; Talbot, J.C. The O and H Stable Isotope Composition of Freshwaters in the British Isles. 2. Surface Waters and Groundwater. *Hydrol. Earth Syst. Sci.* **2003**, *7*, 183–195. <https://doi.org/10.5194/hess-7-183-2003>.
92. Darling, W.G.; Talbot, J.C. The O and H Stable Isotope Composition of Freshwaters in the British Isles. 1. Rainfall. *Hydrol. Earth Syst. Sci.* **2003**, *7*, 163–181. <https://doi.org/10.5194/hess-7-163-2003>.
93. Defliese, W.F.; Lohmann, K.C. Non-Linear Mixing Effects on Mass-47 CO<sub>2</sub> Clumped Isotope Thermometry: Patterns and Implications. *Rapid Commun. Mass Spectrom.* **2015**, *29*, 901–909. <https://doi.org/10.1002/rcm.7175>.
94. Kato, H.; Amekawa, S.; Kano, A.; Mori, T.; Kuwahara, Y.; Quade, J. Seasonal Temperature Changes Obtained from Carbonate Clumped Isotopes of Annually Laminated Tufas from Japan: Discrepancy between Natural and Synthetic Calcites. *Geochim. Cosmochim. Acta* **2019**, *244*, 548–564. <https://doi.org/10.1016/j.gca.2018.10.016>.
95. Létolle, R.; Gégout, P.; Moranville-Regourd, M.; Gaveau, B. Carbon-13 and Oxygen-18 Mass Spectrometry as a Potential Tool for the Study of Carbonate Phases in Concretes. *J. Am. Ceram. Soc.* **1990**, *73*, 3617–3625. <https://doi.org/10.1111/j.1151-2916.1990.tb04267.x>.
96. Böttcher, M.E.; Neubert, N.; Escher, P.; von Allmen, K.; Samankassou, E.; Nägler, T.F. Multi-Isotope (Ba, C, O) Partitioning during Experimental Carbonatization of a Hyper-Alkaline Solution. *Geochemistry* **2018**, *78*, 241–247. <https://doi.org/10.1016/j.chemer.2018.01.001>.
97. Zeebe, R.E. Oxygen Isotope Fractionation between Water and the Aqueous Hydroxide Ion. *Geochim. Cosmochim. Acta* **2020**, *289*, 182–195. <https://doi.org/10.1016/j.gca.2020.08.025>.
98. Weise, A.; Kluge, T. Isotope Exchange Rates in Dissolved Inorganic Carbon between 40 °C and 90 °C. *Geochim. Cosmochim. Acta* **2020**, *268*, 56–72. <https://doi.org/10.1016/j.gca.2019.09.032>.
99. Uchikawa, J.; Zeebe, R.E. The Effect of Carbonic Anhydrase on the Kinetics and Equilibrium of the Oxygen Isotope Exchange in the CO<sub>2</sub>–H<sub>2</sub>O System: Implications for Δ18O Vital Effects in Biogenic Carbonates. *Geochim. Cosmochim. Acta* **2012**, *95*, 15–34. <https://doi.org/10.1016/j.gca.2012.07.022>.
100. Danckwerts, P.V.; Lannus, A. Gas-Liquid Reactions. *J. Electrochem. Soc.* **1970**, *117*, 369C. <https://doi.org/10.1149/1.2407312>.
101. Blunden, J.; Arndt, D.S. State of the Climate in 2018. *Bull. Am. Meteorol. Soc.* **2019**, *100*, Si-S306. <https://doi.org/10.1175/2019BAMSStateoftheClimate.1>.
102. Francey, R.J.; Allison, C.E.; Etheridge, D.M.; Trudinger, C.M.; Enting, I.G.; Leuenberger, M.; Langenfelds, R.L.; Michel, E.; Steele, L.P. A 1000-Year High Precision Record of δ<sup>13</sup>C in Atmospheric CO<sub>2</sub>. *Tellus B* **1999**, *51*, 170–193. <https://doi.org/10.1034/j.1600-0889.1999.t01-1-00005.x>.
103. Cerling, T.E. The Stable Isotopic Composition of Modern Soil Carbonate and Its Relationship to Climate. *Earth Planet. Sci. Lett.* **1984**, *71*, 229–240. [https://doi.org/10.1016/0012-821X\(84\)90089-X](https://doi.org/10.1016/0012-821X(84)90089-X).
104. Dreybrodt, W.; Buhmann, D. A Mass Transfer Model for Dissolution and Precipitation of Calcite from Solutions in Turbulent Motion. *Chem. Geol.* **1991**, *90*, 107–122. [https://doi.org/10.1016/0009-2541\(91\)90037-R](https://doi.org/10.1016/0009-2541(91)90037-R).